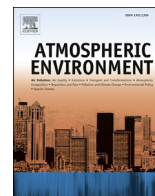# Identification and monitoring of Saharan dust: an inventory representative for south Germany since 1997

H. Flentje, B. Briel, Christoph Beck, M. Collaud Coen, M. Fricke, Josef Cyrys, Jianwei Gu, Mike Pitz, W. Thomas

Contents lists available at ScienceDirect

Atmospheric Environment

journal homepage: www.elsevier.com/locate/atmosenv

Identification and monitoring of Saharan dust: An inventory representative for south Germany since 1997

H. Flentje [a, *], B. Briel [a], C. Beck [b], M. Collaud Coen [c], M. Fricke [a], J. Cyrys [d, e], J. Gu [d, e], M. Pitz [f], W. Thomas [a]

[a] Deutscher Wetterdienst, Met. Obs. Hohenpeißenberg, D-82383 Hohenpeißenberg, Albin-Schwaiger-Weg 10, Germany
[b] Universität Augsburg, Institut für Geographie, Alter Postweg 118, D-86159 Augsburg, Germany
[c] MeteoSwiss, Aerological Station, Les Invuardes, CH-1530 Payerne, Switzerland
[d] Institute of Epidemiology II, Helmholtz Zentrum München, Ingolstädter Landstr. 1, 85764 Neuherberg, Germany
[e] Environment Science Center, University of Augsburg, Universitätsstr. 1a, 86159 Augsburg, Germany
[f] Bavarian Environment Agency, Bürgermeister-Ulrich-Str. 160, 86179 Augsburg, Germany

HIGHLIGHTS

- Large Ca^{2+} abundance and coarse particle volume (0.5–7 μm) indicate Saharan dust.
- The annual number of Saharan dust days shows no significant trend.
- The relative contribution of dust to total particle mass decreases from 6% to 4%.
- Sahara dust events, detected by different metrics at different stations, are consistent.
- 4 of 5 EU law threshold exceedances (daily PM10 > 50 mg/m^3) are due to Saharan dust.

ARTICLE INFO

ABSTRACT

An inventory of Sahara dust (SD) events at the Hohenpeißenberg Global Atmosphere Watch station (Germany) is presented for the period 1997–2013. Based on daily in-situ measurements, high Ca^{2+}-ion concentrations and large particle volume concentrations at diameters $d_p \approx$ 0.5–7 μm are inferred as indicators for days influenced by SD. The resulting SD catalogue agrees with SD time series from Schneefernerhaus, Augsburg and Jungfraujoch stations. On average, SD occurs in 5–15 SD events (SDE) per year covering about 10–60 days/yr in the mixing layer. SDE exhibit a clear seasonality with spring and early autumn maxima, and typically last for 1–3 days. SDE are equally frequent but more significant at Alpine levels due to lower background. Wet deposition of Ca^{2+} at the surface is little correlated ($R^2 = 0.14$) with particle Ca^{2+} on a daily basis and yields an average annual Ca^{2+} immission of 0.22 ± 0.04 g/m^2 yr, about 40% of which is due to SD. The majority of outstanding weekly Fe and Al depositions are associated with SDE. SD contributes about 0.5 ± 0.1 μg/m^3 to the total particle mass with a decreasing trend from 6% to 4% (−0.1%/yr) in the 1997–2013 period. Except from one, all threshold exceedances according to European legislation (daily PM_{10} > 50 μg/m^3) at Hohenpeißenberg are due to SD. Implications are discussed with respect to SD-related circulation patterns, SD-induced temperature anomalies in weather forecast models and the capability of aerosol models to capture SDE.

1. Introduction

Mineral dust significantly affects weather (Pèrez et al., 2006) and climate (Hansen et al., 1997; Philipona et al., 2009) by altering stratification and surface conditions and by its impact on the formation and droplet size of clouds. This again changes the amount (Andreae and Rosenfeld, 2008) and acidity (DeAngelis and Gaudichet, 1991; Wagenbach et al., 1996) of precipitation. The global dust radiative forcing estimation of [−0.3 to +0.1] W/m^2 has a large uncertainty, caused by the lacking knowledge of particle shape, spatial distribution and optical properties. About 80% of the forcing stems from natural sources. Mineral dust amounts to roughly 75% of the global aerosol load and about 35% of the

* Corresponding author.
E-mail address: Harald.Flentje@dwd.de (H. Flentje).

primarily emitted aerosol mass (Boucher et al., 2013). Roughly half of this originates from the Sahara and is transported across the Atlantic towards South America and Eastern US or across the Mediterranean to Europe (Tegen and Schepanski, 2009; Prospero et al., 2014; Pourmand et al., 2014; Kumar et al., 2014). In Europe, Saharan outbursts are frequently observed and, decreasing towards the north, contribute 5%–30% to the total particle mass (Collaud Coen et al., 2004; Papayannis et al., 2008; Pey et al., 2013). While in southern Europe Saharan dust (SD) causes up to 20 daily threshold exceedances per year w.r.t. the European Directive 2008/50/EC, the contribution is harder to quantify for the middle and north (Pey et al., 2013). Annual mean depositions of SD range from 0.4 to 1 gm^{-2} yr^{-1} in alpine ice cores (Wagenbach and Geis, 1989; DeAngelis and Gaudichet, 1991) to several ten gm^{-2} yr^{-1} in southern Europe (Fiol et al., 2005). Dust episodes may be associated with health risks (Karanasiou et al., 2012) and dispersion of epidemic bacteria (Tobias et al., 2011), but the results are still inconsistent due to sparse data. The European regulation of PM_{10}/$PM_{2.5}$ (Linares et al., 2009), makes dust transport also a political and social-economical issue.

Varying between source regions, about 90 mass-% of SD are aluminosilicates (e.g. illite, kaolinite, montmorillonite), iron oxides (hematite, goethite) and quartz (Sokolik and Toon, 1999). The remaining <10% are mostly calcite and gypsum. Ionic Ca^{2+} and alkalinity (H^+-concentration) have been proposed as SD tracers by Wagenbach et al. (1996). K^+ and Mg^{2+} are found in SD, but also in regional minerals, smoke (K^+) and plant debris (K^+, Mg^{2+}). Besides sea-spray, volcanic ash and pollen, mineral dust is the only prominent coarse mode aerosol and thus dominates the particle volume distribution if the former can be ruled out. Dominance of illite, kaolinite and montmorillonite over hematite reflects in stronger shortwave absorption (Russell et al., 2010; Sokolik and Toon, 1999) and spectral single scattering albedo (Collaud Coen et al., 2004). Little import of mineral dust to Central Europe occurs from outside the Sahara (Küfmann, 2003; Birmili et al., 2007), but occasionally significant amounts may emerge from local soils (Goossens et al., 2001; Lequy et al., 2013) and the carbonate massif of the Northern Calcareous Alps (Küfmann, 2003). The latter is formed by the Main Dolomite, a 1–2 km thick lithostratigraphic unit made of >97% dolomite rock ($CaCO_3 \cdot MgCO_3$), which extends all along the north-eastern Alpine ridge. Eolian sediments from regional sources exhibit a clear seasonality due to snow cover in winter (Küfmann, 2003), but are not yet quantified. Thus, a regional dolomite contribution to dust also results in an association of Ca and Mg, but with a probably larger Mg portion than in SD.

The SD fingerprint is less clear in the lower mixing layer (ML) than at mountain stations or in the free troposphere (FT), where it can be observed largely unmixed by lidars and radiometry. Thus we apply a multi-factorial approach to retrieve and identify faint traces of SD in the largely variable ML aerosol in central Europe. We infer a 17-year SD inventory and compare it to independent SDE compilations at surrounding sites, based on particle composition, particle volume distribution (PVD), optical properties and Positive Matrix Factorization (PMF) analysis (section 3). We study the trend of the SD contribution to TSP (PM_{10}), the ambiguity and frequency of events and their dependence on circulation patterns (section 4). From this we draw implications for human health studies and potential impacts on weather and climate. A summary is given in section 5.

2. Experimental

2.1. Measurement sites

In-situ particle measurements are performed at the Global Atmosphere Watch (GAW) global station Hohenpeißenberg HPB

(47.8°N, 11.0°E, 980 m a.s.l.) and Schneefernerhaus SFH (2650 m a.s.l., 40 km south of HPB) since 1997 and 2010, respectively and are continuously complemented. The HPB is a pre-Alpine hill, sticking out 300 m above the surrounding forest/grassland and represents rural central European conditions while SFH is located on the steep south-exposed slope 300 m below Zugspitze summit at the northern ridge of the German Alps. SFH is often above the ML, particularly in winter (Gilge et al., 2010; Flentje et al., 2010). To evaluate our approach we compare SD observations at HPB, SFH and Augsburg (AUG, 480 m a.s.l., 60 km north of HPB, ≈260,000 inhabitants). The AUG data (Pitz et al., 2011) covers the period 2005–2010 and represents lowland urban conditions. Finally, the covariance with SDE at the Swiss GAW global station Jungfraujoch (JFJ, 46.54°N, 7.98°E, 3580 m a.s.l., 250 km SW of HPB, www.ifjungo.ch) is discussed for the period 2001–2011 w.r.t. large scale dispersion and extension of SD layers, c.f. Collaud Coen et al. (2004).

2.2. Ground based in-situ observations

The size-segregated particle ionic composition is sampled since mid 1997 by a cylindrical 3-stage low-pressure Berner-Impactor BI (Wang and John, 1988), paralleled for bulk-validation by 2–3 μm pore-size quartz/teflon-filters. The samples are analysed by ion-chromatography, currently DIONEX ICS 1000 (http://www.dionex.com), after aqueous extraction (Henning et al., 2002). BI and filter probes can be analysed for SO_4^{2-}, NO_3^-, Cl^-, NH_4^+, Na^+, Ka^+, Mg^{2+}, Ca^{2+} and H^+. The BI is equipped with pre-baked ring-like aluminium foils for each of the three stages and segregates particles into three size fractions from 6 to 1.9 μm, 1.9–0.6 μm, 0.6–0.2 μm (stage I–III), and a terminating backup which collects the smallest and previously bounced particles. The BI sampling interval, initially 24-h on weekdays and 48-h at weekends (alternating Sun/Mon changes), recently had to be reduced owing to staff limitations to 3 samples per week (01/08–04/09 and 08/11–12/13) and temporarily one sample per week (10/12–02/13). Since 2010, sampling is interrupted during fog and rain (identified by >97% RH) to avoid flooding. Daily precipitation samples are analysed by ion-chromatography and also sent to the 'Bayerisches Landesamt für Umwelt' for weekly heavy metal analyses, using Inductively Coupled Plasma-Mass Spectrometry. The inlet is PM_{10} (Digitel), except for total mass and total size distribution measurements. The sample air is heated few degrees to avoid condensation and conditioned to below 40% RH by Nafion driers. Particle size/volume distributions (dN/dlogd, dV/dlogd) are measured by optical particle sizers OPS, LAS-X (Hinds and Kraske, 1986) till 2007 and GRIMM-EDM 190 (www.grimm-aerosol.com) as of 2008. The ranges of LAS-X (0.1–7.5 μm) and EDM 190 (0.25–30 μm) both cover the relevant size range of SD particles $d_p = 0.5$–7 μm.

Particle scattering coefficients σ_{sc} are measured by an integrating 3-λ nephelometer TSI 3562 (Anderson and Ogren, 1998), the absorption coefficient σ_{abs} by a 3-λ particle soot absorption photometer PSAP (Bond et al., 1999) as of 2011 and a 7-λ aethalometer (Arnott et al., 2005) as of 2014. From these the extinction coefficient σ_{ext}, the single scattering albedo (SSA) ($\omega_0 = \sigma_{abs}/(\sigma_{abs} + \sigma_{sc})/\sigma_{ext}$) and the respective Ångström Exponents α_{sc}, α_{abs} and α_{ssa} can be calculated as measures of particle size, colour and brightness. The Ångström Exponent is defined by $\sigma_{sc} \sim \lambda^{-\alpha_{sc}}$, resulting in $\alpha_{sc} = -log(\sigma_{sc,\lambda_1}/\sigma_{sc,\lambda_2})/log(\lambda_1/\lambda_2)$ for scattering and analogous for absorption and SSA.

Quality control is performed by intercomparison of Berner with filter measurements, OPS sub-micron size spectra with Scanning Mobility Particle Sizer SMPS, and between the different photometers. The uncertainties of dV/dlogd, σ_{sc}, σ_{abs}, σ_{ext} and the SSA for the relevant SD conditions are of the order of 5–10%. Uncertainties of the chemical data depend on the ion, the sample volume,

interferences and the filter charge/type and, based on regular inter-comparisons (http://qasac-americas.org/), typically range near 20–30%. The detection limit has no impact on our classification since only large values of the primary quantities are important – for Ca^{2+} it is near 10 ng/m^3. Thus analysis limitations are negligible compared to ambiguities w.r.t. the identification of SD and thus may be disregarded. An impact of the data coverage on the detection skill is unavoidable but is reduced by calculating SD through averaging several indicators.

3. Methodology

3.1. Identification of SD by multi-factorial index

Characteristic properties of Saharan air change during transport and are masked by dilution and mixing after entrainment into the ML. Both, fresh and aged SD have frequently been investigated w.r.t. its chemical (DeAngelis and Gaudichet, 1991; Lequy et al., 2013), micro-physical (Weinzierl et al., 2011) and optical properties (Collaud Coen et al., 2004; Müller et al., 2011). See Ansmann et al. (2011) and references therein. Indicators proposed for aged SD are firstly high abundance of Ca^{2+} combined with low H^+-concentration and a K^+/Na^+ ratio larger than 2 (Wagenbach et al., 1996). Secondly, pure SD exhibits a pronounced coarse particle mode (Weinzierl et al., 2011), particle density around 2.6 g/m^3 (Tegen and Fung, 1995), low volatility and hygroscopicity (Weinzierl et al., 2011), enhanced shortwave spectral absorption (Petzold et al., 2011) and negative SSA Ångströms (Collaud Coen et al., 2004). The K^+ criteria cannot be used in the ML due to interferences from fire smoke and plant debris. Alkalinity (background $H^+ \approx 2.4 \pm 4.2$ ng/m^3) and density are too unspecific properties of soils and change by neutralisation (SO$_4$, NO$_3$), coating and mixing. Typical ranges of the relevant criteria during SDE are listed in Table 1.

Owing to the lacking specificity of SD indicators, we use a multiple factor approach to calculate a Sahara dust index 'SDI', however using only the most specific factors to avoid an adverse effect of the less specific ones. So far, only the Ca^{2+} concentration and the particle volume distribution dV/dlogd anomaly turn out as reliable enough in our data (see discussion of spectral absorption below). Thus, the SDI is an *extensive* measure (i.e. depending on particle concentration and particle properties) composed of a volume- and a composition portion $SDI = SDI_{PVD} + SDI_{Ca++}$, comprising presence, concentration and ambiguity of SD. A Saharan dust event 'SDE' (lasting for one or more Saharan dust days 'SDD') occurs if a threshold SDI is exceeded, whereby this value is not fixed but must be determined in the context of each specific application, for example depending on whether misses or false alarms are more critical. To define the SDI, first the fingerprint of SD at HPB was determined from clearly identified SDE. Then frequency distributions during these SDE were filtered in order to iteratively infer

individual thresholds or algebraic relations for single factors, which best distinguish values during SDE from pre-and post-event conditions. Finally, depending on the specificity, individual weights were assigned.

3.1.1. Ca^{++} and H^+-concentration

Daily samples from SDE are enriched in Ca^{2+} ions on BI stages I + II (0.6–6 μm) and the H^+-concentration is low, i.e. the dissolved pH tends to be alkaline. While Ca concentrations exceed 100 ng/m^3 only on ≈ 12 SDD/yr, Ca may also be received from marine, anthropogenic and regional terrestrial sources (Küfmann, 2003; Lequy et al., 2013). The marine contribution Ca_{ss} to total Ca mass is estimated from Na as a reference (Negrel and Roy, 1998), using average global seawater mass ratios Ca/Na ≈ 0.038 from Savenko (1976): $Ca_{ss} = 0.038$Na, and correspondingly for the other ions. Though the median Ca_{ss} contribution during SDD is about 0.3% (all sample median: 1.8%) only, we always refer to non sea-salt calcium fraction Ca_{nss} in the following. The potential non-salt Na fraction (e.g. NaCO$_3$/soda from laundry) is excluded by limiting the Na-reference to the stoichiometric Na/Cl mass ratio in seawater (Na$_{ss}$ < 0.55Cl). Though road salt or coincidences of Cl from a nearby paper factory and NaCO$_3$ would feign marine Ca, this contribution is negligible. Anthropogenic tracers SO_4^{2-} and NO_3^- are weakly correlated with Ca during most SDE, indicating only a small contribution from human sources. Mg vs Ca exhibits two separate branches appearing at large Mg or Ca values: On SDD Mg/Ca ≈ 0.1, while on non-SDD Mg/Ca ≈ 1 roughly corresponds to dolomite. However, most values lie within these extremes and thus do not provide a clear relation for assigning particles to SD or the regional massif. Ca from agriculture mostly re-suspends close to the source (Goossens et al., 2001), confirmed by the absence of local contributions even during the droughty convective summer period in 2003.

Frequency distributions of Ca^{2+} for SD and non-SD periods in Fig. 1 illustrate the suitability of Ca as a measure of strength of SDE, which is largely determined by dilution. Filtering by larger Ca concentration selects more significant SDD at the expense of more misses, and vice versa, but there is no distinct threshold. The Ca background at Hohenpeißenberg is about $Ca_{BG} \approx 25 \pm 20$ ng/m^3(Fig. 1), thus Ca^{2+} < 45 ng/m^3 denotes no significant SDE. Against this, less than 4% of non-SDD exhibit Ca^{2+} > 100 ng/m^3. The overlap of blue (non-SD) and brown (SD) curves depicts ambiguous concentration ranges. Comparing the dashed (stage I only) and solid curves shows that the separation is better based on sizes >0.6 μm (stages I + II) than only on large particles >1.9 μm (stage I). Thus the Ca portion of our daily SD-Index is defined as $SDI_{ca++} = Ca^{2+}_{I+II}*0.01$.

Table 1
Primary criteria for SD identification discussed in the literature and applied in this article (italic). 'Observed parameter' denotes the measured quantity, 'Relevant criterion' denotes the SD criterion derived from the measurement. 'Threshold' is the background or specific value indicating SD.

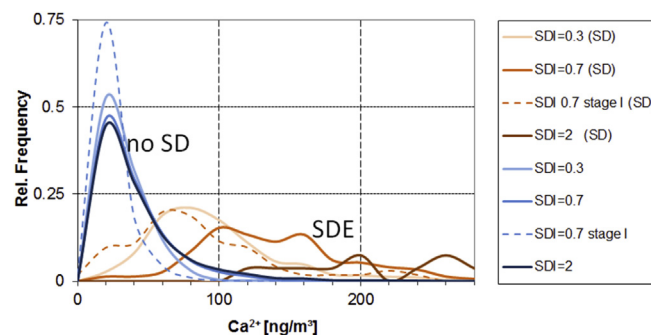| Observed parameter	Relevant criterion	Threshold
Particle volume 0.3–7 μm	$V_p - V_{p,30d-av}$	>6 μm^3/cm^3
Ca^{2+} concentration	$Ca^{2+}_{0.6-6\mu m}$	>30 ng/m^3
pH	H^+/acidity	<<1 ng/m^3
Scattering Ångström exp.	α_{sc}	<0.5
Absorption Ångström exp.	α_{abs}	$\alpha_{abs,blue} >> \alpha_{abs,red}$
SSA Ångström exp.	α_{ssa}	<0

Fig. 1. Relative frequency distributions of Ca^{2+} concentrations observed on SDD and non-SDD, each normalised to the sum of respective days. Different SDI and particle size ranges are distinguished, whereby BI stages I + II are totalised unless noted as 'stage I'. More Ca^{2+} respective higher SDI mean more significant SD influence. Owing to the extended sampling intervals after July 2011, only the preceding period is used.

The scale factor 0.01 weights the Ca portion equal to the size portion (next paragraph).

3.1.2. Size

During SDE the particle volume distribution $dV/dlogd$ is enhanced in the size range $d_p = 0.3–7$ μm, being up to 6 times higher at $1–2$ μm. The presence of SD typically coincides with marked concentration jumps of particles in this size range and mostly negligible contributions from other coarse particles. Thus the volume portion of the daily SDI is calculated from $V_p = \int_{0.3\ \mu m}^{7\ \mu m} (dV/dlogd)dlogd$, offset-corrected by its 30-day running median: $SDI_{PVD} = (V_p - V_{p,30d-av})^*0.1 = V_{p-p30d}^*0.1$. Missing volume distribution data (~7%) is approximated empirically by scattering Ångström exponents α_{sc} via: $SDI_{PVD} \approx SDI_A = 2\alpha_{sc} + 2$, but α_{sc} ($\propto r^2$) is stronger affected by small particles than V_p ($\propto r^3$). α_{sc} ranges from $\alpha_{sp} < 1.5 \pm 0.3$ to $\alpha_{sp} \approx 0.6 \pm 0.2$ during SDE, depending on their significance, while the overall median $\alpha_{sc} \approx 1.85$.

Frequency distributions of the volume criterion (Fig. 2), distinguished for 'weak' (SDI 0.3–0.7), 'moderate' (SDI 0.7–2) and 'strong' (SDI > 2) SDE, show that the long-term background median of $V_{p-p30d,0.3-7\mu m,BG} = 1.1 \pm 3.9$ μm^3/cm^3 is exceeded significantly (>5.0 μm^3/cm^3) in 45%, 78% and 100% of events, respectively. Accordingly, ~30% of 'strong' SDE exceed $V_{p,30d-av}$ only by $6–20$ μm^3/cm^3 (dark brown in Fig. 2) but reach larger SDI > 2 due to high Ca abundance, while days with low Ca and $6–20$ μm^3/cm^3 are classified as non-SDD (~4% of all). Defining days with SDI < 0.3 as non-Saharan, 4 μm^3/cm^3 are never exceeded on non-SDD, but 50% of SDD with SDI = 0.3–0.7 show values below 4 μm^3/cm^3. Small volume anomalies with higher Ca may occur in pure but strongly diluted SD air masses, while enhanced SDI_{PVD} and small Ca suggests contribution from other sources. Possible interferences of small biological particles (pollen, spores, plant debris, …) are identified by their large sizes >>7 μm, but large accumulation mode particles within the SD size range occasionally increase $V_{p-p30d,0.3-7\mu m}$ and limit the specificity of the size criterion.

3.1.3. Absorption

SD reflects in more negative absorption Ångström exponents ($\sigma_{abs} \sim \lambda^{-\alpha_{abs}}$) between 0.37 and 0.59 μm than at longer wavelengths (Collaud Coen et al., 2004). Optically dominating large particles cause scattering Ångström exponents $\alpha_{abs} \approx 0$. SSA correspondingly exhibit negative Ångström exponents α_{ssa} during SDE. At HPB shortwave α_{abs} becomes exceptional negative only during strong SDE like in May 2014 when ground-level SD mass concentrations were >100 μg/m^3 (Table 2), while mixing masks most SDE with less than ≈ 20 μg/m^3 SD contribution in the lower ML. Even at JFJ, where SD arrives largely unmixed, almost half of the SDE show no clear signature in absorption (Collaud Coen et al., 2004). Thus we can detect the SD-characteristic SSA at HPB only since measurements of UV absorption at 370 nm started with a 7-λ aethalometer and can not use this criterion for our long-term SD inventory.

3.2. Assessment of the SDI

3.2.1. Consistency of criteria and locations

The Ca- and the size-criterion for SD identification are highly correlated with coefficients of r = 0.7–0.8 for different periods. Only in the warm year 2003 unusual high Ca^{2+} concentrations in spring combined with moderate coarse particle volumes lead to a lower correlation r = 0.5. Varying Ca- and coarse particle concentrations in SD air-masses result from differing source regions and size modifications during transport, as both are not causally linked. The higher temporal resolution of the size data allows to identify also transient SDE or intermittent entrainment of SD into the ML, not shown by daily averages of Ca concentrations. According to its definition the abundance of SD tracers increases linearly with the SDI. Both, Ca and V_{p-p30d}, are extensive quantities, depending on particle characteristics and -concentration, while α_{ssa} is an intensive quantity and, in the absence of mixing, depend only on particle characteristics. Thus, it is independent from dilution but also affected by admixtures in the ML.

The consistency of this SD inventory with SD compilations from the stations SFH, AUG and JFJ is studied to assess the information content of different criteria. At SFH a SDI_{PVD} is obtained for 2010–2013 from OPS data like at HPB. At AUG the SD-related particle volume distribution is derived from a SMPS and an Aerodynamic Particle Sizer by means of a positive Matrix Factorisation (PMF) analysis for 2005–2010 (Paatero, 1999; Pitz et al., 2011; Gu et al., 2011). The JFJ series is based on the spectral slope of the SSA (Collaud Coen et al., 2004). An additional cross-check with prominent aerosol layers in the free troposphere (backscatter profiles) provides valuable information about the vertical distribution of SD/SDE. Trajectories, satellites, and aerosol models can not generally be applied for verification. Trajectories become unreliable if transport takes longer than several days. Aerosol transport models often provide good qualitative SD information due to realistic sources and transport, but, regarding the substantial inter-model differences, still should be evaluated. An evaluation with AOD (e.g. AERONET) suffers from intermittent data coverage due to clouds and missing vertical resolution, while satellite SD retrievals, as checked for Infrared Atmospheric Sounding Interferometer (IASI) data (not shown), lack sensitivity near the surface and have specificity-, representativeness- and coverage-issues.
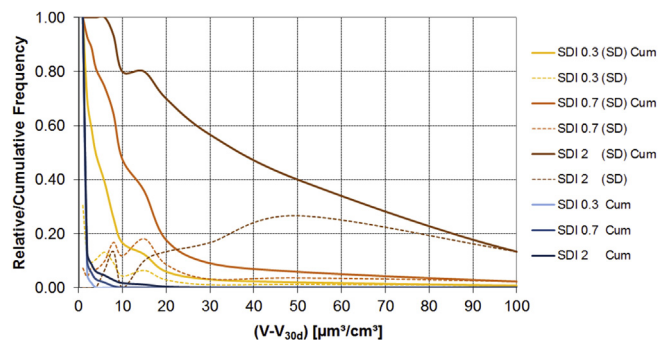

Fig. 2. Cumulative (solid lines) and relative (dashed, normalised to 100%) frequency distributions of the particle volume concentration criterion $V-V_{30d-av} = (SDI_{PVD}^*10)$, separate for days classified as SDD of different significance (brown) and non-SDD (blue).

Table 2
Variation of the spectral absorption before, during and after a strong SDE from 19 to 25 May 2014, measured by a 7-λ aethalometer (MAGEE, AE-33) and a 3-λ particle soot absorption photometer PSAP. The increase of shortwave α_{abs} during the SDE on 22. May 2014 is less pronounced in PSAP data.

Date	ME-33		PSAP	
	$\alpha_{abs_{370-590}}$	$\alpha_{abs_{590-950}}$	$\alpha_{abs_{468-530}}$	$\alpha_{abs_{530-660}}$
19.05.2014	−1.30	−1.17	−1.36	−1.22
20.05.2014	−1.23	−1.13	−1.21	−1.20
21.05.2014	−1.21	−1.09	−1.35	−1.12
22.05.2014	*−2.54*	*−1.19*	*−2.20*	*−1.74*
23.05.2014	−1.37	−1.04	−1.40	−1.10
24.05.2014	−1.24	−1.07	−1.21	−1.02
25.05.2014	−1.37	−1.19	−1.29	−1.10

Italic type highlights the extraordinary values during Saharan dust events in contrast to before and afterwards.

3.2.2. Positive matrix factorization

The detection of SDE by PMF analysis at AUG (Pitz et al., 2011; Gu et al., 2011) is based on the receptor model PMF 3.0 from the US Environmental Protection Agency (EPA), available free of charge at the EPA webpage (http://www.epa.gov/heasd/research/pmf.html). PMF is a widely applied tool for aerosol source apportionment (Paatero, 1999). The details of our approach have been described by Gu et al. (2011). Based on PVD and aided by trace gas and meteorological data from HPB, two factors related to 'long-range transported dust' and 'coarse particles' are output by the PMF as mass contributions of the single factors to the PM_{10} sample data as a source type and strength apportionment.

4. Results

The days exceeding SDI of 0.4 (beige), 0.7 (orange), and 1 (brown) at HPB are shown in Fig. 3 for the period 1997–2013. Which SDI threshold determines a SDD depends on the acceptable misses and surpluses. Obvious choices are SDI > 0.4, SDI > 0.7 or SDI > 1, which correspond to once or twice the sum of the Ca and V_{p-p30d} background values $BG = Ca_{BG}*0.01 + V_{p-p30d,BG}*0.1 \approx 0.36$ or in case of SDI = 1 the sum of Ca and V_{p-p30d} backgrounds plus standard deviations. The frequency and strength of SDE is enhanced in spring and early autumn. Only few SDD are found in winter when the mid-latitudes are decoupled from the subtropics. This seasonal behaviour agrees with mountain site and lidar observations in the free troposphere (Collaud Coen et al., 2004; Papayannis et al.,
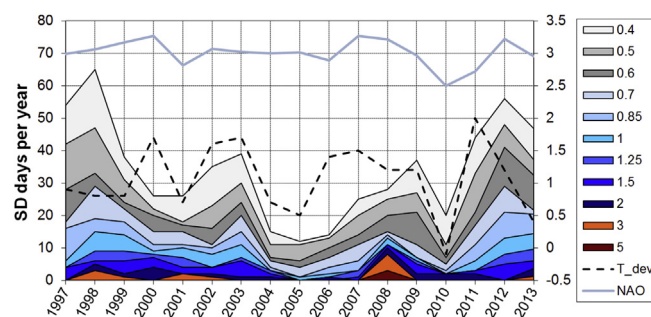

Fig. 4. Number of days per year, exceeding SDI from 0.4 to 5 at HPB in the period 1997–2013. The thick black line 'T-dev' shows the annual temperature deviation from the long-term mean temperature at HPB. The NAO-Index (blue line) is scaled by NAO*0.1 + 3. (For interpretation of the references to colour in this figure legend, the reader is referred to the web version of this article.)

2008). Minutely mass concentrations of SD peak around 100 μg/m³ every few years, but daily averages exceeded 50 μg/m³ only in May 2003, May and October 2008 and in August 2011. The annual count of days exceeding SDI of 0.4–5 at HPB exhibits large interannual variability (Fig. 4), and markedly less SDE in the period from 2004 to 2007 and in 2010.

At HPB on average 5–15 SDE/yr are identified, covering in total 10–60 SDD/yr (35 ± 15 SDD/yr, i.e. $10\% \pm 4\%$) with SDI > 0.4, whereby about 17 ± 8 SDD/yr exceed SDI = 0.7 and 9 ± 5 SDD/yr with SDI > 1 are found. This agrees with findings of Pey et al. (2013)
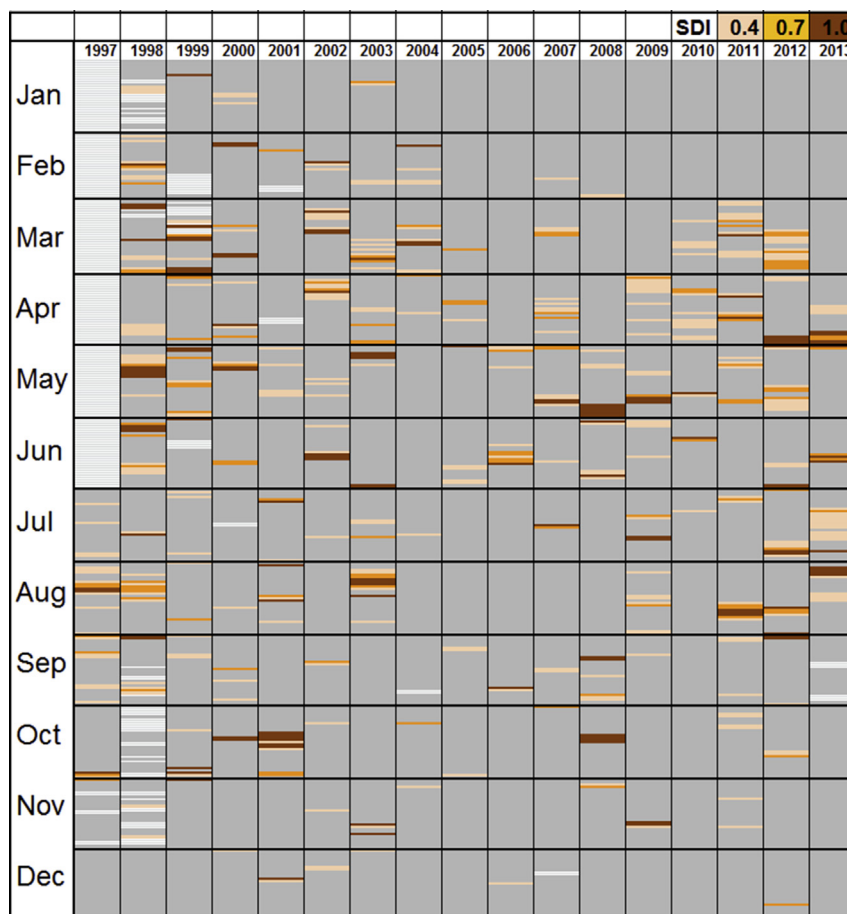

Fig. 3. Inventory of SDD at HPB for the period 1997–2013. Days exceeding a SDI of 0.4, 0.7 and 1.0 are marked in beige, orange and brown. Days with no data are white. (For interpretation of the references to colour in this figure legend, the reader is referred to the web version of this article.)

who used satellite products, dust models and trajectories to identify days influenced by SD and reveal a decrease from more than 130 days (>35%) in the south Mediterranean to less than 60 days (17%) in northern Italy. The drop from 17% to roughly 10% indicates the deflecting effect of the Alps. Owing to the large variability and dry and wet deposition, the annual number of SDD during 1997–2013 does not indicate a significant tendency (-0.28 SDD/yr, $R^2 = 0.03$) but less SDD around 2004–2010 (cf. section 3.3). The annual temperature anomaly at HPB (Fig. 4) is correlated with the frequency of SDE which are typically associated with warm advection. At HPB, 78/96/42/19/9/4/2 SDE (SDI > 0.7) in the 1997–2013 period lasted for 1/2/3/4/5/6/7 consecutive days.

4.1. Wet deposition

Ca in particles and in precipitation samples are only weakly correlated on a daily basis ($R^2 = 0.14$) since rain and mixing of SD down to the surface are not causally linked. The correlation is even less ($R^2 = 0.06$) between SDI and Ca deposition. Observations by a ceilometer network (Flentje et al., 2010) (http://www.dwd.de/ceilomap) show particle layers in the FT over southern Germany on >200 days/yr. Many of them can be detected as SD at the surface, but partly they sway over Germany and reach the surface neither by mixing nor wet deposition. Typically FT layers precede and/or follow the observation of SD at the surface. The combined seasonalities of SD transport to Germany and precipitation produce a strong annual cycle of wet Ca deposition with low values in autumn and winter and a steady increase from March (monthly deposition ≈ 10 mg/m^2) to August (monthly deposition ≈ 50 mg/m^2). Precipitation within ± 1 day around a SDE contains significantly enhanced Ca^{2+} (21% vs 13%), reduced H$^+$ (0.5% vs 1.3%) and slightly increased NO$_3^-$ concentrations (20% vs 16%) than apart SDE (each referred to total ions). On the long term, this leads to a fairly stable annual Ca immission of 0.22 ± 0.04 g/m^2 yr of which on average 0.09 ± 0.01 g/m^2 yr (41%) stems from SD. Likewise Ca, immission of the most abundant metals in SD, Fe and Al, is often missing during dry SDE or occurs without a SD signal at the surface (cf. next section). Yet, on a monthly mean basis, about half of the Fe immission peaks are associated with peaking SDI, while the others may stem from local dust, biomass burning or industrial processes (Mead et al., 2013).

4.2. Comparison of SDI and PMF approach for Hohenpeißenberg (10/10–12/11)

The PMF for HPB data from 10/2010 to 12/2011 yields two factors, 'coarse particles' (CP) and 'long range transported dust' (LRD), which may be associated with mineral dust (Gu et al., 2011) or volcanic ash (Pitz et al., 2011). The PVD of 'CP' and 'LRD' peak around 4 μm and 2 μm, respectively. The factor CP may include both, large particles from regional sources and dust. A weak correlation of CP and LRD ($R^2 = 0.21$) confirms the separation of both factors by the PMF. Missing (anti)correlation of LRD with gaseous tracers (e.g. CO, NO$_x$) indicates mixing with pollutants en route. Spearman correlation coefficients with the SDI are low for CP (0.144) and LRD (0.126). Only one further factor, attributed to 'secondary aerosol' (SA), exhibits a, however negative, association with the SDI, probably due to removal of SA by the relatively large SD surface sink and/or low SA precursor concentrations in the Saharan air. The factor related mass concentration of LRD increases with the SDI and we find a cumulation of higher SDI at high LRD related masses as expected, but also some high SDI with low LRD related masses. This could be cases with relatively small but Ca-rich particles.

4.2.1. Comparison to Schneefernerhaus time series (2011–2013)

About 90% of the SDE at HPB in 2011–2013 are detected within ± 1 day at the SFH as well, while in 96% a SDE at SFH is accompanied within ± 1 day by an event at HPB. The number of days with particle volume anomalies 6 μm^3/cm^3 < V$_{p-p30d}$ < 20 μm^3/cm^3 (SDI$_{PVD}$ < 2, Ca^{2+} is not measured at SFH) is equal at HPB and SFH but the significance of events (larger anomalies or SDI$_{PVD}$) is higher at SFH due to the lower background (Table 3). This means that SD arrives less diluted at SFH but from this level is always mixed down to the lower boundary layer. The superposition of both inventories in Fig. 5 shows that SDE often last longer at HPB due to decelerated advection in the ML.

4.2.2. Comparison to PMF analysis for Augsburg (2005–2010)

AUG is affected by more local sources and less vertical exchange than SFH and HPB, particularly w.r.t. diurnal thermal Alpine circulation (Alpine pumping) and ML inversions. The best coincidence of SDE is reached for a SDI of 0.4 and PMF factor mass of 4 μg/m^3, resulting in the SD coincidences shown in Fig. 6. This is plausible as SDI$_{PVD}$ = 0.4 ≡ 4 μm^3/cm^3 ≡ 4 μg/m^3 for a density of 1 gm^{-3}. Neglecting lags of up to ± 1 day between both stations, we find 135 coincident SDD for the period 2005–2010, while 40 and 41 are only found in Augsburg and HPB, respectively. Strong events are captured by both the PMF for AUG and the SDI for HPB. Only 3 of 37 SDD with SDI > 1 at HPB are not noticeable in Augsburg. Only 1 of 37 days with PMF factor mass >14 μg/m^3 at Augsburg is not detected at HPB. This confirms that SD identification by both methods yields equivalent results, whereby the number of SDD best follows a power law dependence with $N_{SDD} \propto (SDI)^{-1.34}$ respective $N_{SDD} \propto (PMFfactormass)^{-1.44}$. It further suggests that already the diurnal PVD alone captures most SDE.

4.2.3. Comparison to Jungfraujoch time series (2001–2012)

The identification of SDE via the Ångström exponent α_{ssa} at JFJ (Collaud Coen et al., 2004) started in March 2001. The comparability to HPB is limited by the ≈ 250 km distance between JFJ and HPB, the smaller degree of ML air exposure at JFJ, and the different temporal resolution of the metrics (daily Ca^{2+} and V$_p$ at HPB vs hourly α_{ssa} at JFJ). A SDD is identified at JFJ as soon as the SD criterion is fulfilled during four consecutive hours, but the strength of SDE cannot be compared. At JFJ 363/140/76 days are found with $\alpha_{ssa} < 0$ for more than 4 h/12 h/24 h in the period 2001–2012, while at HPB 350/150/79 days are found with a SDI exceeding 0.4/0.7/1. The coincidences of SDE at JFJ and HPB (Table 4) shows that only one third of SDE are detected on the same day, the others are several days delayed or do not reach one of the stations at all. More delays or misses are found for HPB, since SD often arrives from SW and the Alps have a shading effect. On average, SDE last shorter at JFJ than at HPB (like at SFH), because air mass exchange is more inertial in the ML (persistence) than in the FT. Small-scale or dilute plumes loose their clear fingerprint through mixing to lower levels,

Table 3
Number of SDD/yr at HPB and SFH as a function of the SDI, indicating the dependence of the SDI on altitude. At the high altitude site SFH SDE are more significant due to the lower background.

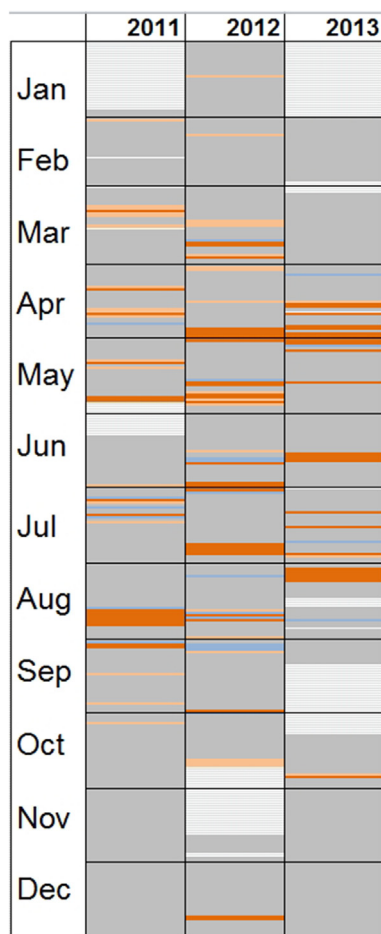| SDI	SDD/yr HPB	SDD/yr SFH
0.5	34	34
0.7	33	31
1	28	28
2	20	21
3	12	16
5	10	15
8	7	12
15	3	7

Fig. 5. Daily inventory of SDD at HPB and SFH from 2011 to 2013. Coincidences are marked brown, misses at SFH light brown, excess SD days (each w.r.t. HPB) blue, zeros in grey and days with no data in white. (For interpretation of the references to colour in this figure legend, the reader is referred to the web version of this article.)

while SDE that cover large parts of the Alps are shown by both records.

4.3. TSP mass contribution from SDE

The contribution of SD to the total suspended particle TSP mass concentration at HPB is calculated from the difference between long-term average TSP with and without SDD (SDI > 0.7). TSP measurement by Tapered Element Oscillating Monitor TEOM misses highly volatile organic particles due to sample air heating to 40 °C, but this has negligible effect on SD. The contribution of SD to TSP varies between 1% and 2% (2005, 2010) and 9%–11% (2003, 2008) and on average amounts to $0.5 \pm 0.3\ \mu g/m^3 (5.0 \pm 2.3\%)$ of the long-term average ($10.4\ \mu g/m^3$), about the same as the black carbon (soot) fraction. In presence of a decreasing TSP trend ($-0.22\ \mu g/m^3\ yr$, $R^2 = 0.7$), the SD contribution also shows a decreasing trend from $0.7\ \mu g/m^3 (5.9\%)$ to $0.4\ \mu g/m^3 (4\%) (-0.1\%/yr, R^2 = 0.04)$ from 1997 to 2013. The uncertainty due to missed SDE is small as events with high mass concentrations are captured reliably and false alarms are very few. The sensitivity can thus be estimated to be about $0.1\ \mu g/m^3$ by varying the SDI threshold between 0.4 and 1. It turns out that at HPB all except one threshold exceedances of daily TSP ($\equiv PM_{10}$) $\mu g/m^3$ according to the EU Directive 2008/50/EC are due to presence of SD. The exception was an inversion pollution event with immissions from the Bohemian industrial area in Feb
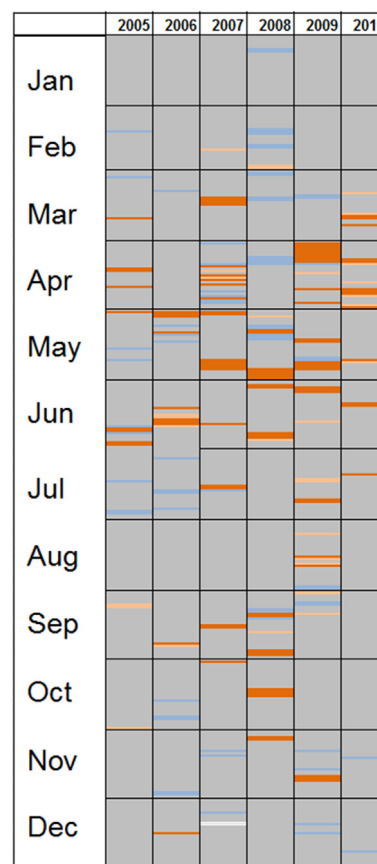

Fig. 6. Coincidences of SD days at HPB and AUG from 2005 to 2010 as in Fig. 5.

Table 4
Relative frequency of coincident SDE at HPB and JFJ. Upper line: Days on which a SDE is detected at JFJ given there is one at HPB. Lower line: Days on which a SDE is detected at HPB given there is one at JFJ. Here, SDI > 0.7 defines a SDD at HPB, α_{ssa} being negative for more than 12 h defines a SDD at JFJ.

	±5d	±4d	±3d	±2d	±1d	±0d
SDE @ HPB	0.71	0.67	0.63	0.57	0.49	0.3
SDE @ JFJ	0.54	0.53	0.51	0.47	0.43	0.28

2012. These results are valid for PM_{10}, too, which apart from pollen episodes corresponds to TSP, as $d_{p,SD} < 7\ \mu m$ at HPB.

5. Discussion

The proposed method to infer SDD is simple and widespread applicable since measurements of PVD and/or Ca^{2+} are commonly performed by environmental agencies. This makes it suitable for operational SD monitoring, particularly in the ML. Its information content equals a PMF as shown by the comparison to the analysis for Augsburg for the period 2005–2010. From the different moments (mean, diurnal cycle, directionality) taken into account by the PMF, the daily mean PVD is the decisive one. For NRT monitoring and assimilation into models it offers less complexity and higher time resolution than chemical analysis. The same holds for spectral absorption measurements covering the UV, which offers the additional advantage of being an intensive quantity. From hitherto experience, we expect the absorption (or SSA) from 370 to 950 nm by the Magee Scientific, AE33 aethalometer (instead of 467–660 nm with the − discontinued − PSAP), to provide about the

same selectivity to SD as the PVD and Ca. Discrepancies between PMF and SDI analysis for HPB are likely caused by the brevity of the analysed period (10/2010–12/2011) with exceptional SD transports across the North Atlantic (e.g. 10–12 April 2011), as indicated by an enhanced SD-related factor contribution from northerly directions.

The consistency of the SDI with SDE at neighboured stations and different approaches (PMF and α_{ssa}) confirms the method and representativeness of this SD inventory for southern Germany. The seasonality, frequency of SDD and mass contribution of SD to TSP (PM$_{10}$) are in line with recent publications. Long-term studies for the Mediterranean region (Moulin et al., 1998; Pey et al., 2013), are extended to the north. The decrease from 37% SDD/yr (Sicily) to 17% (Northern Italy), reported by Pey et al. (2013), continues to 10% ± 4% over southern Germany. This marked drop is interpreted as a deflective impact of the Alps which is also suggested by the differences between SDE at HPB and JFJ. The observed decreasing trend of the SD mass contribution to TSP from 6% to 4% firstly extends the aerosol phenomenology of Putaud et al. (2010), who infer 5–10% of mineral dust (without trend analysis) in average PM$_{10}$ chemical composition for 60 European stations but state an uncertainty for dust apportionment of ±150% due to different mineral dust formulae based on Ca, but also Si, Al, Fe, Mg and others. Secondly, it confirms the decreasing dust-PM$_{10}$ trend found by Pey et al. (2013) in the NW Mediterranean from 2006 onward, there attributed to the increasingly negative North Atlantic Oscillation (NAO) index (southward displacement of the storm track, decoupling sub-tropics and mid-latitudes).

The seasonality of SDE (Fig. 3) is associated with circulation types (or general weather situations) that lead to pronounced SD events. As an experiment we classified 500 hPa geopotential height (GPH) fields for days with strong SD influence (SDI > 1) by non-

hierarchical k-means cluster analysis (Hartigan, 1975). By this, 4 main circulation types have been extracted whose centroid patterns (GPH composites) are displayed in Fig. 7. The majority of summer and autumn events result from different circulation patterns than the spring cases. While in spring SDE tend to be associated with stronger zonal currents over north Africa and troughs over western and southwestern Europe, SDE in autumn are by the majority induced by ridging over north-eastern Africa and the Mediterranean. The main transport paths correspondingly shift from the east Mediterranean (zonal transport over Africa) towards west during the year (blocking high in the east) as asserted by (Moulin et al., 1998).

Owing to the manifold relevance of SD, a long-term SDI inventory may further be utilized for model evaluation, health and immission studies in central Europe. The influence of SDE on the forecast error in the German Meteorological Agency Local Model LM is evident for the strong SDE from 26 to 30 May 2008, when dust AOD was $\tau_{max} \approx 0.7$ over central Europe and hourly surface PM$_{10}$-concentrations exceeded 100 μg/m^3. Larger than usual deviations of the 0–72 h forecast from the analyses are found when regions inside and outside the SD are compared before (20–24 May 2008), during (25–30 May 2008) and after (31 May–04 June 2008) the main event. By about 1–2 °C larger temperature anomalies occur while the model run is degraded by the SD. An even larger effect can be expected with higher model resolution, when the periods and regions influenced by SD can be optimally chosen. In order to reduce such errors, weather forecast models presently start to integrate aerosols like the MACC (Monitoring of Atmospheric Composition and Climate) integrated forecasting system (Morcrette et al., 2011), but a correct aerosol load is indispensable to realistically reproduce SD-induced cloud condensation, heating
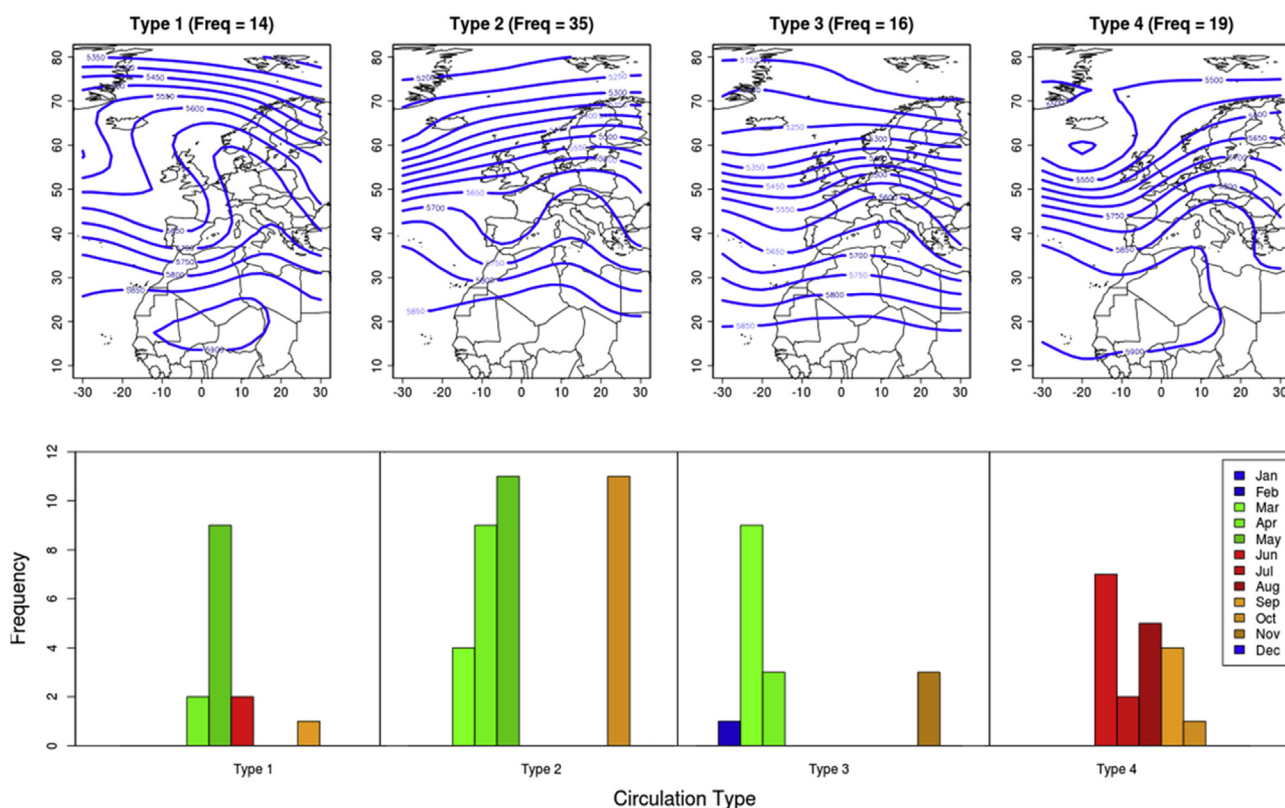

Fig. 7. Top: 500 hPa geopotential height composites for the main circulation types from cluster analysis of 500 hPa geopotential height fields on days with SDI > 1. Below: Monthly frequency of occurrence of the 4 circulation types.

or cooling. For example, it can be shown that the MACC model (AOD_{550nm}) captures all SDD with SDI > 1 at HPB, while weaker events are more often missed. Lofted SD layers often remain for long in the FT without being mixed to the ground. A comprehensive evaluation of long-range aerosol transport in the MACC model is beyond the scope of this article. Epidemiological studies suggest an association of SDE with cardiovascular and respiration diseases but the results are still inconsistent due to sparse data and the variety of stress factors that interfere with human health (Karanasiou et al., 2012). The measured SD immission of 0.09 ± 0.01 g/m^2 yr Ca is negligible as agricultural fertiliser (≈ 0.9 kg/ha), but the alkaline compounds may have a relevant buffering effect on acid soils in sensitive regions like upland moors. This topic will be studied in more detail with mass profiles estimated from the DWD ceilometer network (Flentje et al., 2010), which yields SD annual depositions of similar magnitude as the surface observations.

6. Conclusions

Surface aerosol measurements at the GAW global station Hohenpeißenberg (Germany) are used to infer a catalogue of Saharan dust events SDE over southern Germany during the period 1997–2013. The most specific SD tracers are daily Ca^{2+}-ion concentration, acidity (H^+) and particle volume distribution, while absorption and SSA are sensitive for SD only at short wavelengths <450 nm. From the further, a Saharan dust index SDI is calculated as a measure of daily SD abundance SDI = $(V_p - V_{p,30d-av})$ *0.1 + Ca^{2+}*0.01 for particles with 0.3–7 μm diameter. The specificity of the criteria is validated by good agreement with SD series from surrounding stations. Depending on the significance, we identify SD in 5–15 annual events, covering 10–60 days/yr at ground level. SDE are equally frequent but more significant at Alpine levels due to lower background. SDE are more frequent in spring and late summer/early autumn, and typically last for 1 to 3, but up to 7 consecutive days. The SD contribution to PM$_{10}$ is about 0.5 ± 0.1 μg/m^3 and exhibits a decreasing trend from 6% to 4% (−0.1%/yr) of the decreasing PM$_{10}$ (−0.22 μg/m^3/yr, $R^2 = 0.7$). The SDI catalogue is applied to detect SD-induced temperature anomalies in DWD Local Model forecasts and to confirm the capability of the ECMWF MACC model to capture significant SDE.

Acknowledgements

References

Anderson, T., Ogren, J., 1998. Determining aerosol radiative properties using the TSI 3563 integrating nephelometer. Aerosol Sci. Tech. 29 (1), 57–69.

Andreae, M., Rosenfeld, D., 2008. Aerosol-cloud-precipitation interactions. Part 1. The nature and sources of cloud-active aerosols. Earth Sci. Rev. 89, 13–41.

Ansmann, A., Petzold, A., Kandler, K., Tegen, I., Wendisch, M., Müller, D., Weinzierl, B., Müller, T., Heintzenberg, J., 2011. Saharan mineral dust experiments SAMUM-1 and SAMUM-2: what have we learned? Tellus 63B, 403–429.

Arnott, W., Hamasha, K., Moosmüller, H., Sheridan, P., Ogren, J., 2005. Towards aerosol light-absorption measurements with a 7-wavelength Aethalometer: evaluation with a photoacoustic instrument and 3-wavelength nephelometer. Aerosol Sci. Tech. 39 (17), 17–28.

Birmili, W., Schepanski, K., Ansmann, A., Spindler, G., Tegen, I., Wehner, B., Nowak, A., Reimer, E., Mattis, I., Müller, K., Brüggemann, E., Gnauk, T., Herrmann, H., Wiedensohler, A., Althausen, D., Schladitz, A., Tuch, T., Löschau, G., 2007. A case of extreme particulate matter concentrations over central Europe caused by dust emitted over the southern Ukraine. Atmos. Chem. Phys. 8, 997–1016.

Bond, T., Anderson, T., Campbell, D., 1999. Calibration and intercomparison of filter-based measurements of visible light absorption by aerosols. Aerosol Sci. Tech. 30 (6), 582–600.

Boucher, O., Randall, D., Artaxo, P., Bretherton, C., Feingold, G., Forster, P., Kerminen, V.M., Kondo, Y., Liao, H., Lohmann, U., Rasch, P., Satheesh, S.K., Sherwood, S., Stevens, B., Zhang, X.Y., 2013. Clouds and aerosols. In: Stocker, T.F., Qin, D., Plattner, G.-K., Tignor, M., Allen, S.K., Boschung, J., Nauels, A., Xia, Y., Bex, V., Midgley, P.M. (Eds.), Climate Change 2013: the Physical Science Basis. Contribution of Working Group I to the Fifth Assessment Report of the Intergovernmental Panel on Climate Change. Cambridge University Press, Cambridge, United Kingdom and New York, NY, USA.

Collaud Coen, M., Weingartner, E., Schaub, D., Huglin, C., Corrigan, C., Henning, S., Schwikowski, M., Baltensperger, U., 2004. Saharan dust events at the Jungfraujoch: detection by wavelength dependence of the single scattering albedo and first climatology analysis. Atmos. Chem. Phys. 4, 2465–2480.

DeAngelis, M., Gaudichet, A., 1991. Saharan dust deposition over Mont Blanc (French Alps) during the last 30 years. Tellus 43B, 61–75.

Fiol, L., Fornós, J., Gelabert, B., Guijarro, J., 2005. Dust rains in Mallorca (Western Mediterranean): their occurrence and role in some recent geological processes. Catena 63, 64–84.

Flentje, H., Claude, H., Elste, T., Gilge, S., Köhler, U., Plass-Dülmer, C., Steinbrecht, W., Thomas, W., Werner, A., Fricke, W., 2010. The Eyjafjallajökull eruption in April 2010 detection of volcanic plume using in-situ measurements, ozone sondes and lidar-ceilometer profiles. Atmos. Chem. Phys. 10, 1008510092.

Gilge, S., Plass-Duelmer, C., Fricke, W., Kaiser, A., Ries, L., Buchmann, B., Steinbacher, M., 2010. Ozone, carbon monoxide and nitrogen oxides time series at four alpine GAW mountain stations in central Europe. Atmos. Chem. Phys. 10, 1229512316.

Goossens, D., Gross, J., Spaan, W., 2001. Aeolian dust dynamics in agricultural land areas in Lower Saxony, Germany. Earth Surf. Process. Landforms 26, 701–720.

Gu, J., Pitz, M., Schnelle-Kreis, J., Diemer, J., Reller, A., Zimmermann, R., Söntgen, J., Stölzel, M., Wichmann, H.-E., 2011. Source apportionment of ambient particles: comparison of positive matrix factorization analysis applied to particle size distribution and chemical composition data. Atmos. Environ. 45, 1849–1857.

Hansen, J., Sato, M., Ruedy, R., 1997. Radiative forcing and climate response. J. Geophys. Res. 102 (D6), 6831–6864.

Hartigan, J., 1975. Clustering Algorithms. Wiley Series in Probability and Mathematical Statistics. New York, p. 351.

Henning, S., Weingartner, E., Schwikowski, M., Gaeggeler, H., Gehrig, R., Hinz, K., Trimborn, A., Spengler, B., Baltensperger, U., 2002. Seasonal variation of the water soluble ions of the aerosol at the high-Alpine site Jungfraujoch (3580 m a.s.l.). J. Geophys. Res. 107.

Hinds, W., Kraske, G., 1986. Performance of PMS model LAS-X optical particle counter. J. Aerosol Sci. 17, 67–72.

Karanasiou, A., Moreno, N., Moreno, T., Viana, M., de Leeuw, F., Querol, X., 2012. Health effects from Sahara dust episodes in Europe: literature review and research gaps. Environ. Int. 47, 107–114.

Küfmann, C., 2003. Soil types and eolian dust in high-mountainous karst of the Northern Calcareous Alps. Catena 51, 211–227.

Kumar, A., Abouchami, W., Galer, S., Garrison, V., Williams, E., Andreae, M., 2014. A radiogenic isotope tracer study of transatlantic dust transport from Africa to the Caribbean. Atmos. Environ. 82, 130–143.

Lequy, E., Nicolas, M., Conil, S., Turpault, M.P., 2013. Relationship between atmospheric dissolved deposition and mineral dust deposition in French forests. Water Air Soil Pollut. 224, 1680.

Linares, C., Diaz, J., Tobias, A., 2009. Are the limit values proposed by the new European Directive 2008/50 for PM2.5 safe for health? Eur. J. Public Health 19 (4), 357–358.

Mead, C., Herckes, P., Majestic, B., Anba, A., 2013. Source apportionment of aerosol iron in the marine environment using iron isotope analysis. Geophys. Res. Lett. 40, 5722–5727.

Morcrette, J., Benedetti, A., Jones, L., Kaiser, J., Razinger, M., Suttie, M., 2011. Prognostic aerosols in the ECMWF IFS: MACC vs. GEMS aerosols. ECMWF Tech. Memo. 659, 32.

Moulin, C., Lambert, C., Dayan, U., Masson, V., Ramonet, M., et al., 1998. Satellite climatology of African dust transport in the Mediterranean atmosphere. J. Geophys. Res. 103, 13137–13144.

Müller, T., Schladiz, A., Kandler, K., Wiedensohler, A., 2011. Spectral particle absorption coefficients, single scattering Albedos, and imaginary parts of refractive indices from ground-based in-situ measurements at Cape Verde Island during SAMUM2. Tellus 63B.

Negrel, P., Roy, S., 1998. Chemistry of rainwater in the Massif Central (France): a strontium isotope and major element study. Appl. Geochem. 13 (8), 941–952.

Paatero, P., 1999. The multilinear engine – a table-driven, least squares program for solving multilinear problems, including the η-way parallel factor analysis

model. J. Comput Graph Stat. 8, 854−888.

Papayannis, A., Amiridis, V., Mona, L., 2008. Systematic lidar observations of Saharan dust over Europe in the frame of EARLINET (2000−2002). J. Geophys. Res. 113, D10204.

Petzold, A., Veira, A., Mund, S., Esselborn, M., Kiemle, C., Weinzierl, B., Hamburger, T., Ehret, G., Lieke, K., Kandler, K., 2011. Mixing of mineral dust with urban pollution aerosol over Dakar (Senegal): impact on dust physico-chemical and radiative properties. Tellus 63B, 619634.

Pey, J., Querol, X., Alastuey, A., Forastiere, F., Stafoggia, M., 2013. African dust outbreaks over the Mediterranean Basin during 2001−2011: PM10 concentrations, phenomenology and trends, and its relation with synoptic and mesoscale meteorology. Atmos. Chem. Phys. 13, 1395−1410.

Pèrez, C., Nickovic, S., Pejanovic, G., Baldasano, J., Özsoy, E., 2006. Interactive dust-radiation modeling: a step to improve weather forecasts. J. Geophys. Res. 111, D16206.

Philipona, R., Behrens, K., Ruckstuhl, C., 2009. How declining aerosols and rising greenhouse gases forced rapid warming in Europe since the 1980s. Geophys. Res. Lett. 36, L02806.

Pitz, M., Gu, J., Soentgen, J., Peters, A., Cyrys, J., 2011. Particle size distribution factor as an indicator for the impact of the Eyjafjallajökull ash plume at ground level in Augsburg, Germany. Geophys. Res. Lett. 11, 93679374.

Pourmand, A., Prospero, J., Sharifi, O., 2014. Geochemical fingerprinting of trans-Atlantic African dust based on radiogenic Sr-Nd-Hf isotopes and rare earth element anomalies. Geology 42 (8), 675−678. http://dx.doi.org/10.1130/G35624.1.

Prospero, J., Collard, F.X., Molinie, J., Jeannot, A., 2014. Characterising the annual cycle of African dust transport to the Caribbean basin and South America and its impact on the environment and air quality. Glob. Biogeochem. Cycles 29, 757−773.

Putaud, J.P., Van Dingenen, R., Alastuey, A., Bauer, H., Birmili, W., Cyrys, J., Flentje, H., Fuzzi, S., Gehrig, R., Hansson, H., Harrison, R., Herrmann, H., Hitzenberger, R., Hüglin, C., Jones, A., Kasper-Giebl, A., Kiss, G., Kousam, A., Kuhlbusch, T., Löschau, G., Maenhaut, W., Molnar, A., Moreno, T., Pekkanen, J., Perrino, C., Pitz, M., Puxbaum, H., Querol, X., Rodriguez, S., Salma, I., Schwarz, J., Smolik, J.,

Schneider, J., Spindler, G., ten Brink, H., Tursic, J., Viana, M., Wiedensohler, A., Raes, F.A., 2010. European aerosol phenomenology − 3: physical and chemical characteristics of particulate matter from 60 rural, urban, and kerbside sites across Europe. Atmos. Environ. 1−13.

Russell, P., Bergstrom, R., Shinozuka, Y., Clarke, A., De Carlo, P., Jimenez, J.L., Livingston, J., Redemann, J., Dubovik, O., Strawa, A., 2010. Absorption Angstrom Exponent in AERONET and related data as an indicator of aerosol composition. Atmos. Chem. Phys. 10, 11551169.

Savenko, V., 1976. Chemical composition of atmospheric precipitations over oceans. Geokhimiya 12, 1890−1893.

Sokolik, I., Toon, O., 1999. Incorporation of mineralogical composition into models of the radiative properties of mineral aerosol from UV to IR wavelengths. J. Geophys. Res. 104, 9423−9444.

Tegen, I., Fung, I., 1995. Contribution to the atmospheric mineral aerosol load from land surface modification. J. Geophys. Res. 100 (D9), 18707−18726.

Tegen, I., Schepanski, K., 2009. The global distribution of mineral dust. IOP Conf. Ser. Earth Environ. Sci. 7.

Tobias, A., Cayla, J., Pey, J., Alastuey, A., Querol, X., 2011. Are Saharan dust intrusions increasing the risk of meningococcal meningitis? Int. J. Infect. Dis. 15 (7).

Wagenbach, D., Geis, K., 1989. In: Leinen, M., Sarnthein, M. (Eds.), The Mineral Dust Record in a High Altitude Alpine Glacier (Colle Gnifetti, Swiss Alps): Paleoclimatology and Paleometeorology: Modern and Past Patterns of Global Atmospheric Transport), pp. 543−564.

Wagenbach, D., Preunkert, S., Schäfer, J., Jung, W., Tomadin, L., 1996. Northward transport of Saharan dust recorded in a deep alpine ice core. In: Guerzoni, S., Chester, R. (Eds.), The Impact of Desert Dust Across the Mediterranean. Kluwer Academic Publishers, pp. 291−300.

Wang, H., John, C., 1988. Characteristics of the berner impactor for sampling inorganic ions. Aerosol Sci. Tech. 8 (2), 157−172.

Weinzierl, B., Sauer, D., Esselborn, M., Petzold, A., Veira, A., Rose, M., Mund, S., Wirth, M., Ansmann, A., Tesche, M., Groß, S., Freudenthaler, V., 2011. Microphysical and optical properties of dust and tropical biomass burning aerosol layers in the Cape Verde region: an overview of the airborne in situ and Lidar measurements during SAMUM2. Tellus 63B (4), 589618.